Susceptibility-Based Neuroimaging: Standard Methods, Clinical Applications, and Future Directions

Salil Soman, MD, MS,
Department of Radiology, Beth Israel Deaconess Medical Center, Harvard Medical School, Rosenberg 90A, 1 Deaconess Road, Boston, MA 02215, Tel: 617-754-2009

Jose A. Bregni, MD,
Universidad Francisco Marroquin, Guatemala

Berkin Bilgic, PhD,
Department of Radiology, Massachusetts General Hospital, Harvard Medical School, A.A. Martinos Center for Biomedical Imaging 149 13th Street, Room 2.102, Charlestown, MA 02129, Tel: 617-866-8740

Ursula Nemec, MD,
Department of Radiology, Medical University of Vienna, Austria

Audrey Fan, PhD,
Department of Radiology, Stanford School of Medicine 300 Pasteur Dr, MC 5105, Stanford, CA94305

Zhe Liu, BS,
Cornell MRI Research Lab, Cornell University, 515 East 71st St, Suite 104, New York, NY 10021, Phone: (646) 962-2640, Zl376@cornell.edu

Robert L. Barry, PhD,
Department of Radiology, Massachusetts General Hospital, Harvard Medical School, A.A. Martinos Center for Biomedical Imaging 149 13th Street, Suite 2.301, Charlestown, MA 02129 USA, Tel: 615-801-0795

Jiang Du, PhD,
Department of Radiology, UCSD, 200 West Arbor Drive, San Diego, CA 92103-8226, Tel: 619-471-0519

Keith Main, PhD,
Principal Scientist (SME), Research Division, Defense and Veterans Brain Injury Center, General Dynamics Health Solutions, 1335 East-West Hwy, Suite 4-100, Silver Spring, MD 20910

Jerome Yesavage, MD, PhD,

Department of Psychiatry & Behavioral Sciences, Stanford School of Medicine, Mail Code 151-Y, 3801 Miranda Avenue, Palo Alto, California 94304, Phone (650) 852-3287

Maheen M Adamson, PhD,
Department of Neurosurgery, Department of Psychiatry & Behavioral Sciences, Stanford School of Medicine, Defense and Veterans Brain Injury Center, VA Palo Alto Health Care System (PSC/117), 3801 Miranda Avenue (151Y), Palo Alto, CA 94304

Michael Moseley, PhD, and
Department of Radiology, Stanford School of Medicine, Mail Code 5488, Route 8, Rm PS059, Stanford, CA, 94305-5488, Tel: 650-725-6077 moseley@stanford.edu

Yi Wang, PhD
Department of Radiology, Cornell Medical School, Department of Biomedical Engineering, Cornell University, 301 Weill Hall, 237 Tower Road, Ithaca, NY 14853, Tel: 646 962-2631

Abstract

The evaluation of neuropathologies using MRI methods that leverage tissue susceptibility have become standard practice, especially to detect blood products or mineralization. Additionally, emerging MRI techniques have the ability to provide new information based on tissue susceptibility properties in a robust and quantitative manner. This paper discusses these advanced susceptibility imaging techniques and their clinical applications.

Keywords

neuropathologies; MRI; neuroimaging; susceptibility imaging techniques

Introduction

A variety of adult and pediatric neuropathologies demonstrate abnormal accumulation of blood products or mineralization, critical to diagnosis. While CT based methods can detect larger hemorrhages and mineralization, smaller lesions, such as microhemorrhages, may only be visible on MRI. In general, MRI is more sensitive than CT in the detection of hemorrhage at all stages of parenchymal hematoma evolution. A spectrum of MRI pulse sequences leveraging tissue susceptibility are in routine clinical use, with many emerging techniques becoming more available. In this paper we will review the spectrum of techniques available, their clinical applications, and future directions for susceptibility imaging.

Structural Susceptibility Imaging

The sensitivity of MRI to even small hemorrhages is due to its ability to depict susceptibility effects within tissues. The susceptibility of a tissue is a proportionality constant that indicates the degree of magnetization in response to an applied magnetic field. Negative susceptibility is termed diamagnetism and positive susceptibility is paramagnetism (Table 1). If two tissue regions have different magnetic susceptibility, a spatially varying magnetic field is induced in the space surrounding the tissue interface or structure, causing protons there to

precess around the main field B_0 at different rates (also known as dephasing), resulting in T2* decay. Therefore, tissue structure can be depicted on T2* weighted imaging (T2*w) but in an amplified blooming hypointensive contrast.

A common susceptibility MRI in routine clinical practice utilizes a T2*w 2D gradient echo sequence (2D GRE). 2D GRE applies a readout pre-phasing gradient that dephases the spins, which are then rephased using a readout gradient with opposite polarity. A peak signal, i.e. echo, occurs at the echo time (TE) when the total area under the readout gradient is equal to zero. This process takes advantage of the fact that the main magnetic field (B_0) created is inhomogeneous throughout the tissue and experiences a T2* decay as the molecules are dephasing. The total dephasing of the hydrogen molecules depends on the strength of the magnetic field and the echo time duration. TEs in the range of 15 to 20 ms with 3–5 mm thick sections are used in clinical 2D gradient-echo imaging. Longer TEs of ~25 ms are less common because of the signal-intensity loss associated with rapid phase changes across a voxel. Signal-to-noise ratio can be significantly improved using the 3D implementation of GRE (3D GRE) that acquires all sections simultaneously [1]. 3D GRE has been demonstrated to depict greater sensitivity to susceptibility differences when imaging at higher resolution, which requires longer scan times[2]. Multishot, multiecho acquisitions are able to obtain multiple TEs per repetition time (TR)(Figure 1).

In contrast to GRE magnitude only images, phase information has signed values that are opposite for paramagnetic and diamagnetic structures, allowing blood products to be distinguished from calcification. These phase maps, proportional to the magnetic field multiplied by TE, are influenced by both intravoxel and extravoxel susceptibility sources, i.e., do not reflect local tissue property [1]. Additionally, phase maps have been noted to demonstrate orientation dependence.[3]

Susceptibility Weighted Imaging (SWI) uses phase image information about local susceptibility changes between tissues[4] to further attenuate signal or enhance the hypointensive contrast using a phase mask [5]. SWI has been shown to be 3–6 times more sensitive than 2D GRE in detecting size, number, volume, and distribution of hemorrhagic lesions in Diffuse Axonal Injury (DAI).[6–8] However, the enhanced prominence of vessels can also obscure pathological lesions[9].

Quantitative susceptibility mapping (QSM) images depict local tissue's susceptibility value, in contrast to the above traditional GRE contrasts (SWI, Phase and T2*w) that do not exclusively depict local tissue magnetic property, but rather a weighted sum of magnetic properties of adjacent tissues. This blooming contrast or artifacts in traditional GRE are especially problematic at air-tissue interfaces, across which large susceptibility changes are present, greatly distorting images. QSM uncovers local tissue magnetic properties by deconvolving the inhomogeneity field map with the unit dipole kernel that relates susceptibility distribution and the field. The inversion from measured magnetic field to the underlying susceptibility, which is ill-posed due to zeroes in the dipole kernel (7,8) and was hindered by streaking artifacts in early attempts of simple kernel division (9,10), has been successfully achieved using the Bayesian approach [10–12]. Tissue structural information as defined on anatomic images is used to select a unique susceptibility solution of minimal

streaking for a given field. Numerous implementations by various groups have consistently demonstrated that the Bayesian approach allows robust and reliable QSM [13–16]. Benefits of this QSM method include not only providing field and echo time independent susceptibility measurement, but also the depiction of paramagnetic and diamagnetic structures with opposite signal, enabling the differentiation of blood products from calcification.

Functional Susceptibility Imaging

BOLD Contrast—Increased neural activity within a cerebral area produces local biochemical changes that result in increased blood flow in order to meet the oxygen demand. [17] The increase of blood flow washes out deoxyhemoglobin (dhb) with oxyhemoglobin (ohb); dhb is a paramagnetic substance, and so produces a substantially higher signal decay than ohb, resulting in a relative increase in signal as the concentration of dhb is reduced. This phenomenon is known as the Blood Oxygenation Level Dependent signal (BOLD) contrast.[18] Changes in the BOLD contrast over time can be used with a variety of functional paradigms to infer information about brain activity. Examples include task response and resting state analyses.

Dynamic Susceptibility Contrast (DSC) Enhanced MR Perfusion—DSC MR perfusion, or perfusion-weighted imaging, demonstrates brain perfusion data by imaging circulation of contrast (which is paramagnetic) within the brain using serial T2 or T2* weighted MRI. The susceptibility effect of the contrast agent causes signal loss, and using the principles of indicator dilution theory, the signal information can then be converted into a contrast concentration– time curve across all imaged voxels. Cerebral blood volume (CBV) and flow (CBF) parametric maps can be derived from this data. Additionally, regional CBF and CBV values can be produced by analyzing regions-of-interest. [19]

Ultrasmall / Superparamagnetic Iron Oxide (USPIO/SPIO) Nanoparticles

USPIOs / SPIOs are Iron oxide nanoparticles with T1 and T2 shortening and T2* decreased signal which can be administered intravenously, to evaluate anatomic and physiologic facets of pathology. Depending on the tumor type, USPIO/SPIOs can cross areas of blood brain barrier breakdown. After hours to days, USPIO/SPIOs are taken up by macrophages, at which time the particles demonstrate a marked T2 and T2* effect but markedly diminished T1 effect relative to its interstitial phase.[20]

Clinical Applications

Traumatic Brain Injury (TBI)

An estimated 1.7 million people sustain a TBI in the US annually.[21] While CT remains the gold standard for the initial evaluation in fast detecting hemorrhages,[22] SWI enhances contrast in hemorrhagic foci and helps depict localization, volume and number of injuries. [22, 23] Size of lesions might appear larger on SWI than on T1 or T2 weighted images because of the susceptibility effect of hemoglobin degradation. SWI has been shown to be more sensitive for evaluation of microhemorrhages in the brainstem and corpus callosum than CT, T2, T2* and FLAIR imaging.[6, 24–26] SWI may be considered as a valuable tool

for patient follow-up because imaging methods, like CT and conventional MRI, are less sensitive for evaluating evolving and small hemorrhagic lesions.[23, 27] The number and volume of hemorrhagic lesions have been noted to correlate with Glasgow Coma Scale (GCS) scores, with brainstem lesions correlating especially well with GCS.[25, 26, 28]

Seizures—SWI has demonstrated decreased cerebral vein signal within 2 hours after ending of seizure episodes, resulting in patches of nonvisualized cortical veins. [29] Similarly, nonvisualization of cortical veins on SWI with corresponding areas of hyperperfusion on DSC perfusion MRI has been shown in patients with seizures.[30]

Demyelinating disorders

Multiple Sclerosis (MS) accounts for nearly 95% of all cases of demyelinating diseases,[31] and is characterized by multi focal demyelination and iron deposition throughout the brain and spinal cord, resulting in altered tissue susceptibility, visible on GRE, SWI and QSM imaging.[32] Susceptibility-based techniques, such as SWI and QSM, have demonstrated many white and grey matter MS lesions with a central vein, highlighting their perivenular localization.[33] Natalizumab, an effective treatment for relapsing-remitting MS, carries the risk for developing progressive multifocal leukoencephalopathy (PML). PML can be seen as increased susceptibility in U-fibers or deep gray matter on T2*, SWI or QSM, which may be due to iron deposition.[34]

Infectious diseases

Brain abscesses and intracranial infections are visible on SWI. While early Syphilis central nervous system (CNS) invasion is seen in 40% of patients, neurological symptoms occur in only a minority of patients.[35, 36] Widespread cortical asymmetric bilateral hypointensities on SWI with no correlation on conventional sequences was demonstrated in a small series of immunocompetent patients with progressive cognitive decline. [36]

Abscesses have been shown to demonstrate more routine dual rim configuration than glioblastoma multiforme (GBM) on SWI.[37] A dual-rim sign consists of two concentric rims surrounding the central cavity at lesion margins, with the outer ring hypointense and the inner ring hyperintense relative to the cavity content on SWI. This dual-rim sign has also been noted specifically in pyogenic abscesses, but not in fungal abscesses using SWI. This work found fungal abscesses to have a prominent single peripheral rim or central susceptibility and that, especially for aspergillus colonies, intralesion low SWI signal was present. This low SWI signal may represent aggregation of iron and magnesium essential for hyphal growth. [38]

Complications of bacterial meningitis include intracranial vascular involvement: ischemic and hemorrhagic complications, sinus thrombosis and microbleeds. In the setting of bacterial meningitis, SWI low intensity signals represent deoxyhemoglobin, hemorrhagic blood products and methemoglobin, which are often not visible on CT.[39]

GRE and SWI can provide information about prenatal or postnatal parasitic infections by localizing hemorrhage or cerebrovascular complications associated with infectious agents. Cytomegalovirus (CMV) may demonstrate periventricular calcifications; rubella may show

periventricular white matter, basal ganglia and brainstem necrosis, gliosis and calcification; toxoplasmosis can demonstrate basal ganglia, periventricular or cerebral parenchyma calcifications; neurocysticercosis can demonstrate calcifications and hemorrhage. Viral agents such as herpes type 2 can demonstrate temporal, hippocampal and limbic system hemorrhage. Cerebral malaria may produce diffuse brain parenchyma hemorrhages. While CT is an imaging technique that is sensitive to calcification and larger hemorrhages, SWI can detect small and early changes, and avoid the use of ionizing radiation to this population.[40]

Stroke—SWI has been shown to be more sensitive to intra-infarct hemorrhage than CT and GRE.[41] SWI also allows early detection of hemorrhagic transformation of stroke.[42–44] The presence of intra-arterial thrombus can present on GRE/SWI as intra-arterial low signal and vessel diameter enlargement relative to the contralateral vessel, also termed as "the susceptibility sign".[41, 43] Infarct/peri-infarct tissue can also demonstrate differences in perfusion parameters secondary to steno-occlusive disease using DSC perfusion.[45]

Hemodynamic compromise in stroke can also be depicted as paucity of veins in the region of infarct. Uncoupling of oxygen supply and demand in hypoperfused tissue may cause increased dhb relative to ohb in the tissue capillaries and draining veins, which will be demonstrated as prominent hypointense draining veins on SWI.[22]

Similar to adults, hypointense prominent draining veins for hypoperfused tissue on SWI can help identify area of infarct in children. However, hyperintense venous signal on SWI can indicate areas of hyperperfusion, which are associated with increased risk of post ischemic malignant edema.[40, 42]

SWI's ability to detect microbleeds (hypointense dots smaller than 5mm) make it useful in the evaluation of subacute to chronic strokes, perinatal vascular insults, chronic hypertension, cerebral autosomal dominant arteriopathy, subacute infarcts and leukoencephalopathy (CADASIL), cerebral amyloid angiopathy, vasculitis, infective endocarditis, and Binswanger's disease, all of which increase the risk of stroke.[41]

Adult and pediatric studies have also demonstrated that mismatch between areas of SWI and diffusion weighted imaging (DWI) were able to similarly identify patients at increased risk for infarct growth as the mismatch between perfusion weighted imaging (PWI) and DWI. [42, 46] These results suggest that SWI-DWI mismatch may be useful in patients who cannot receive contrast for PWI.

Vascular Malformations—Arteriovenous Malformations (AVM) are one of the most common causes of spontaneous intracranial hemorrhage and is defined as arteries connected with veins without a capillary bed in-between.[47] While the gold standard for detection, morphology evaluation and hemodynamics of vascular malformations is digital subtraction angiography (DSA),[47–49] the invasive nature of the procedure makes noninvasive diagnostic alternatives desirable. Compared to GRE, SWI provides better visualization of low-flow vascular malformations, which can be not visible on GRE.[50] SWI enhances the blooming effect of venous blood and provides a detailed visualization of low flow lesions,

like cerebral cavernous malformations (CCM). CCM lesions have dhb, which is paramagnetic, resulting in decreased SWI signal intensity. One study found that 44% of the CCM detected by SWI were not seen on GRE. [51] Similarly SWI has been shown to be superior to GRE for detection of capillary telangiectasias, and for the ability distinguishing these entities from more serious pathologies such as metastasis.[52]. A limitation of SWI is that evaluation of anatomy may be challenging in presence of microbleeds because both the feeding artery and draining vein have low intensity signal.[47] Also, high-flow anomalies may not be visible on SWI.[49] Vein of Galen aneurysm malformation is a condition where choroidal arteries drain directly into median prosencephalic vein, often with neonatal period congestive heart failure. SWI can provide information to differentiate between low flow and high flow abnormalities of the vein of Galen. [53]

Sturge-Weber-Dimitri Syndrome (SWS) is a condition defined by facial capillary, ipsilateral glaucoma and abnormal capillary venous vessels in the leptomeninges (pial or leptomeningeal angiomas).[40, 54] SWI has been shown superior to standard T1 post contrast MRI for demonstrating abnormal transmedullary veins, periventricular veins, cortical gyriform hypointensities and gray white junction abnormalities. SWI can also detect white matter and cortical calcifications, as well as decreased venous oxygen due to chronic venous ischemia and venous stasis.[40, 55–57] SWS associated lesions, such as enlarged choroid plexus and leptomeningeal angiomas, was shown to be better visualized on post contrast T1 imaging than on SWI.[58]

Venous Sinus Thrombosis—The overall reduced brain perfusion seen in cerebral venous sinus thrombosis (CVST) can manifest as hypointense and / or engorged sulcal veins and collateral slow flow on SWI in the region of ischemia. [59] SWI can also depict brain hemorrhage that occurs after venous thrombosis.[54]

Neoplasms—SWI helps in tumor detection by defining tumor boundaries, architecture of tumoral vascularization and presence of hemorrhages.[60] Delimitation of the peripheral tumoral invasion zone with high vascularity has improved using contrast-enhanced SWI.[61] Human and animal studies have shown even more detailed delineation using targeted superparamagnetic contrast agents using contrast enhanced SWI (CE-SWI). [61] Particles can cross the blood-brain barrier and then get phagocytized by tumor associate macrophages (TAMs). USPIOs have been demonstrated to detect and quantify TAMs.[62]

Intratumoral calcifications are evident in a variety of glioma subtypes: oligodendroglioma, ganglioglioma, pilocytic astrocytoma and ependymoma.[61]

The intratumoral development of calcification is considered a positive response to treatment while new intratumoral susceptibility signal (ITSS) is concerning for recurrent or progressive disease. As the tumoral grade increases, the neovascularity also increases, and also, with a higher grade glioma microhemorrhages from rupture of abnormal vessels and necrosis due to higher cell growth and inability to maintain tumoral cell metabolism. Dot or linear ITSS represent neoangiogenic vessels, conglomerated areas represent micro hemorrhage and necrosis. The pattern of ITSS correlates with the WHO histological grades.

[61, 63] QSM's ability to distinguish calcification from blood products make it well suited to evaluate response to therapy.

Similar to adults, SWI helps in identification of hemorrhage, calcification and vascularity within pediatric tumors, thereby providing information about tumor grade, treatment and prognosis.[54, 55] Calcification indicate slower growth and may define a lower grade, whereas in rapid growing tumors may present with hemorrhage or necrosis.[54] SWI can be helpful for early detection of basal ganglia germinomas because of the increased concentration of blood products and biologic metal within the tumoral bed.[63] In neurooncology, CBV is the most robust and widely used DSC perfusion parameter. [64]

Procedures—Neuronavigation-guided frameless stereotactic biopsy (NSTB) by MRI is a minimally invasive method for obtaining brain tumor samples.[65] The most common complications are hemorrhage and intracranial hypertension secondary to bleeding. SWI can reveal small vessels for preoperative planning, including trajectory to avoid vessels or tumor vasculature, reducing post-operative complications. [65]

Deep brain stimulation into the globus paliidus interna, subthalamic nucleus or the ventral intermediate nucleus is indicated for Parkinson's, tremor disease and dystonia. SWI can visualize cerebral vascular structures and has been shown to improve target identification. [66] Additionally, QSM imaging has been demonstrated to depict greater contrast to noise ratio in targeting the subthalamic nucleus (STN).[67]

Spinal Cord—Spinal cord edema is associated with a favorable neurological outcome whereas hemorrhage has poor neurological recovery. SWI exploits the susceptibility effects and makes hemorrhages detectable and is far superior to detect microbleeds than T2WI or T2*WI. Scan time is relatively short, giving the opportunity to include this sequence in MRI protocol for spinal cord injured patients.[68] An example of spine susceptibility imaging is the MERGE (multi-echo recombined gradient echo) acquisition, with typical scan parameters of: TR range, 950–1000; bandwidth, 31 kHz; matrix, 288 × 192; slice thickness, 3 mm; 1-mm skip; FOV, 20×20 cm; and number of signals acquired, 2).[69] MERGE imaging has been noted to provide greater sensitivity for cord lesions, while traditional axial T2-weighted FSE provided improved lesion specificity.[69]

Anatomy—SWI has been show to identify the structure and oxygen saturation of small spinal veins.[70] As spinal AVMs would be expected to have higher oxygen saturation than other venous structures (due to related increased arterial inflow),[71] the phase information from SWI may help identify AVMs.

Similarly, SWI has been shown to demonstrate brainstem around the brainstem and midbrain well. Example applications include surgical planning for dural arteriovenous fistulas, identification of trigeminal nerve root vascular compression, and evaluating tumor vascular supply. In addition to abnormal structures, SWI can demonstrate venous drainage of the brainstem and for pre-surgical planning.[72]

Future Directions

An inherent limitation to QSM is that its production is defined by an ill-posed linear system, requiring spatial regularization that imposes sparsity or smoothness assumptions. Example QSM reconstruction methods include MEDI[10, 73, 74], HEIDI[75], and compressed sensing (CS).[76] An alternative approach to these single orientation methods is acquiring additional GRE volumes at multiple head orientations (calculation of susceptibility through multi-orientation sampling -COSMOS). This multi-orientation sampling relies on the fact that, as the head is rotated inside the receive array, the dipole kernel also moves relative to the main magnetic field.[77] This acquisition scheme allows the undersampled frequency content of the susceptibility map to vary as a function of rotation and enables dipole inversion through the solution of an over-determined linear system. COSMOS has been shown to provide higher quality estimates than regularized QSM from a single orientation. [73, 78] COSMOS has also been shown to yields exquisite detail and contrast at ultra high field.[79, 80]

A hindrance to acquiring multi-orientation imaging is prohibitively long scan times, which are proportional to the number of orientations sampled. Parallel imaging, a set of techniques that employ receiver sensitivity encoding to reconstruct images from undersampled k-space acquisitions,[81–83] can allow faster acquisitions for each volume. While conventional parallel imaging allows up to 3-fold acceleration with good image quality, exploiting the fact that 3D-GRE for QSM acquisitions employs two axes for phase encoding (ky and kz) allows even greater acceleration (performed along both axes). Controlled Aliasing in Parallel Imaging (2D-CAIPI) is one such implementation. [84] Wave-CAIPI[85] combines 2D-CAIPI with Bunch Encoding[86] to permit an order of magnitude acceleration with small noise amplification and image artifact penalties. When applying these methods to QSM, overall scan time can be enhanced by applying the efficient trajectories of Echo planar imaging (EPI), which encodes an entire kx-ky plane following a single RF excitation, and can be extended to allow 3D-EPI by phase encoding along kz dimension.[87] The combination of 3D-EPI with 2D-CAIPI allows up to 16-fold acceleration while flexibly trading speed for reduced distortion.[87] 3D-EPI QSM has been demonstrated to produce 1 mm isotropic images in 30 seconds [88], and 3D-Spiral QSM has produced 1 mm resolution images in 2.5 minutes.[89] Applying Wave-CAIPI acquisition to COSMOS has demonstrated 15-fold accelerated Wave-CAIPI protocol that allowed 0.5 mm isotropic resolution from a total 20 min scan at 3 head orientations at 7T,[90] with faster scan times possible at lower resolution.

A challenge to clinical implementation of QSM arises from its background field removal methods. Assumptions implicit in most background field removal methods resulting in imprecise separation of background and tissue fields. This issue is particularly prominent near the brain boundary, where large tissue–air susceptibility differences are present[13]. To avoid the separate fitting of background and local field, Laplacian-based QSM methods have been developed[10, 91]. However, the implementation of the Laplacian requires some compromise between robustness against error amplification and the integrity of the visualized cortical brain tissue[76]. The total field inversion preconditioned QSM method (TFI) has been recently demonstrated to reduce the error propagation associated with

imprecise background field removal, and suppress streaking artifacts in intracerebral hemorrhage on QSM images (Figure 2).[92]

QSM venography / oxygen extraction measurement can also evaluate brain metabolism.[93, 94] Early quantitative studies to measure oxygen saturation typically modeled large draining veins[95] and cortical vessels[96] as long cylinders parallel to the main field. With this assumed geometry and orientation, a simple relation exists between the measured field shift $B_{\text{vein-water}}$ and the oxygen extraction fraction (OEF): $B_{\text{vein-water}} = 4\pi \ \chi_{do0}$ Hct OEF, where χ_{do0} is the susceptibility shift between fully oxygenated and fully deoxygenated blood. However, this approach restricts OEF evaluation to a limited set of vessels with the appropriate geometry, which are manually tasking to identify. Subsequent 3D QSM methods provided sufficient spatial resolution to allow OEF assessment along the entire brain vasculature. The whole brain maps of susceptibility produced, with CSF used as water reference susceptibility, susceptibility shifts and thus OEF can be measured along all vessels to create "quantitative oxygenation venograms" (Figure 3). While this methodology has been tested with physiological gas challenges that change the brain oxygenation state,[97] second order flow effects on the phase signal[98] and partial volume effects can cause underestimation in OEF values. New methods to automatically segment vessels from QSM scans can allow for automated OEF quantification with reduced potential error due to vein tilt angle and partial volume effects[99, 100].

At 7T, susceptibility imaging of the spinal cord using T2* weighted 3D-GRE has been able to delineate MS lesion hyperintensities in high detail. In a cohort of MS patients, a comparison between 3T T2W images and 7T T2* images permitted the detection of 52% more white matter lesions at 7T than at 3T. These results demonstrate the potential benefits of ultra-high field imaging in the detection and monitoring of pathologies that may not be readily visualized at lower fields. [101]

At 7T, resting state BOLD fMRI was also used to demonstrate functional connectivity between left and right ventral (motor) horns, and between left and right dorsal (sensory) horns of spinal cord gray matter (Figure 4).[102] Future work will investigate applications of resting state spinal cord networks in evaluating central nervous system dysfunction in clinical populations.

Ultrashort echo time methods (UTE) have been able to delineate cortical bone in high detail, including throughout the neural axis (Figure 5). In addition to direct imaging, these methods are also being used for attenuation correction in PET-MRI systems.[103] UTE methods have also shown promise in evaluating white matter via myelin selective imaging.[104, 105]

Susceptibility tensor imaging (STI) is an extension of susceptibility mapping that captures the orientation dependence of tissue susceptibility through a tensor model. Similar to diffusion tensor imaging, STI allows mapping of brain white matter fiber orientations and reconstruction of 3D white matter pathways using the principal eigenvectors of the susceptibility tensor. In contrast to diffusion anisotropy, the main determinant factor of the susceptibility anisotropy in brain white matter is myelin.[106]

Conclusions

Susceptibility based imaging methods are able to run provide rich structural and functional information across a variety of neuropathologies. Range of information possible for imaging the neural axis is set to expand greatly, based on new acquisition, reconstruction and post processing methods, as well as the broader availability of iron oxide nanoparticle imaging.

Supplementary Material

Refer to Web version on PubMed Central for supplementary material.

Acknowledgments

References

1. Wang, Y. Principles of Magnetic Resonance Imaging: Physics Concepts, Pulse Sequences, & Biomedical Applications. CreateSpace Independent Publishing Platform; 2012.

2. Vernooij MW, et al. Cerebral microbleeds: accelerated 3D T2*-weighted GRE MR imaging versus conventional 2D T2*-weighted GRE MR imaging for detection. Radiology. 2008; 248(1):272–7. [PubMed: 18490493]

3. Shmueli K, et al. Magnetic susceptibility mapping of brain tissue in vivo using MRI phase data. Magn Reson Med. 2009; 62(6):1510–22. [PubMed: 19859937]

4. Reichenbach JR, et al. Small vessels in the human brain: MR venography with deoxyhemoglobin as an intrinsic contrast agent. Radiology. 1997; 204(1):272–7. [PubMed: 9205259]

5. Haacke EM, et al. Susceptibility-weighted imaging: technical aspects and clinical applications, part 1. AJNR Am J Neuroradiol. 2009; 30(1):19–30. [PubMed: 19039041]

6. Tong KA, et al. Hemorrhagic shearing lesions in children and adolescents with posttraumatic diffuse axonal injury: improved detection and initial results. Radiology. 2003; 227(2):332–9. [PubMed: 12732694]

7. Tong KA, et al. Diffuse axonal injury in children: clinical correlation with hemorrhagic lesions. Ann Neurol. 2004; 56(1):36–50. [PubMed: 15236400]

8. Cheng AL, et al. Susceptibility-weighted imaging is more reliable than T2*-weighted gradient-recalled echo MRI for detecting microbleeds. Stroke. 2013; 44(10):2782–6. [PubMed: 23920014]

9. Soman S, et al. Improved T2* imaging without increase in scan time: SWI processing of 2D gradient echo. AJNR Am J Neuroradiol. 2013; 34(11):2092–7. [PubMed: 23744690]

10. de Rochefort L, et al. Quantitative susceptibility map reconstruction from MR phase data using bayesian regularization: validation and application to brain imaging. Magn Reson Med. 2010; 63(1):194–206. [PubMed: 19953507]

11. Wang Y, et al. Magnetic source MRI: a new quantitative imaging of magnetic biomarkers. Conf Proc IEEE Eng Med Biol Soc. 2009; 2009:53–6. [PubMed: 19965112]

12. Kressler B, et al. Nonlinear regularization for per voxel estimation of magnetic susceptibility distributions from MRI field maps. IEEE Trans Med Imaging. 2010; 29(2):273–81. [PubMed: 19502123]

13. Wang Y, Liu T. Quantitative susceptibility mapping (QSM): Decoding MRI data for a tissue magnetic biomarker. Magn Reson Med. 2015; 73(1):82–101. [PubMed: 25044035]

14. Haacke EM, et al. Quantitative susceptibility mapping: current status and future directions. Magn Reson Imaging. 2015; 33(1):1–25. [PubMed: 25267705]

15. Liu C, et al. Quantitative Susceptibility Mapping: Contrast Mechanisms and Clinical Applications. Tomography. 2015; 1(1):3–17. [PubMed: 26844301]

16. Reichenbach JR, et al. Quantitative Susceptibility Mapping: Concepts and Applications. Clin Neuroradiol. 2015; 25(Suppl 2):225–30.

17. Rigolo L, et al. Development of a clinical functional magnetic resonance imaging service. Neurosurg Clin N Am. 2011; 22(2):307–14. x. [PubMed: 21435578]

18. Ogawa S, et al. Brain magnetic resonance imaging with contrast dependent on blood oxygenation. Proc Natl Acad Sci U S A. 1990; 87(24):9868–72. [PubMed: 2124706]

19. Ostergaard L. Principles of cerebral perfusion imaging by bolus tracking. J Magn Reson Imaging. 2005; 22(6):710–7. [PubMed: 16261573]

20. Iv M, et al. Clinical applications of iron oxide nanoparticles for magnetic resonance imaging of brain tumors. Nanomedicine (Lond). 2015; 10(6):993–1018. [PubMed: 25867862]

21. M, F., et al. Traumatic Brain Injury in the United States: Emergency Department Visits, Hospitalizations and Deaths 2002–2006. N.C.f I.P.a C Centers for Disease Control and Prevention. , editor. Centers for Disease Control and Prevention, National Center for Injury Prevention and Control; Atlanta GA: 2010.

22. Mittal S, et al. Susceptibility-weighted imaging: technical aspects and clinical applications, part 2. AJNR Am J Neuroradiol. 2009; 30(2):232–52. [PubMed: 19131406]

23. Toth A, et al. Microbleeds may expand acutely after traumatic brain injury. Neurosci Lett. 2016; 617:207–12. [PubMed: 26912192]

24. Choi JI, et al. Comparison of subgroups based on hemorrhagic lesions between SWI and FLAIR in pediatric traumatic brain injury. Childs Nerv Syst. 2014; 30(6):1011–9. [PubMed: 24408783]

25. Geurts BH, et al. The reliability of magnetic resonance imaging in traumatic brain injury lesion detection. Brain Inj. 2012; 26(12):1439–50. [PubMed: 22731791]

26. Park JH, et al. Detection of traumatic cerebral microbleeds by susceptibility-weighted image of MRI. J Korean Neurosurg Soc. 2009; 46(4):365–9. [PubMed: 19893728]

27. Sharp DJ, Ham TE. Investigating white matter injury after mild traumatic brain injury. Curr Opin Neurol. 2011; 24(6):558–63. [PubMed: 21986682]

28. Iwamura A, et al. Diffuse vascular injury: convergent-type hemorrhage in the supratentorial white matter on susceptibility-weighted image in cases of severe traumatic brain damage. Neuroradiology. 2012; 54(4):335–43. [PubMed: 21611726]

29. Iwasaki H, Fujita Y, Hara M. Susceptibility-weighted imaging in acute-stage pediatric convulsive disorders. Pediatr Int. 2015; 57(5):922–9. [PubMed: 25922882]

30. Verma RK, et al. Focal and Generalized Patterns of Cerebral Cortical Veins Due to Non-Convulsive Status Epilepticus or Prolonged Seizure Episode after Convulsive Status Epilepticus – A MRI Study Using Susceptibility Weighted Imaging. PLoS One. 2016; 11(8):e0160495. [PubMed: 27486662]

31. Calabresi, PA. Goldman-Cecil Medicine. 25th. Vol. 2. Elsevier; 2016. Multiple Sclerosis and Demyelinating Conditions of The Central Nervous System.

32. Chen W, et al. Quantitative susceptibility mapping of multiple sclerosis lesions at various ages. Radiology. 2014; 271(1):183–92. [PubMed: 24475808]

33. Oztoprak B, Oztoprak I, KYildiz O. The effect of venous anatomy on the morphology of multiple sclerosis lesions: a susceptibility-weighted imaging study. Clin Radiol. 2016; 71(5):418–26. [PubMed: 26966086]

34. Hodel J, et al. Brain Magnetic Susceptibility Changes in Patients with Natalizumab-Associated Progressive Multifocal Leukoencephalopathy. AJNR Am J Neuroradiol. 2015; 36(12):2296–302. [PubMed: 26316568]

35. Khamaysi Z, et al. Clinical and imaging findings in patients with neurosyphilis: a study of a cohort and review of the literature. Int J Dermatol. 2014; 53(7):812–819. [PubMed: 24261864]

36. Pesaresi I, et al. Susceptibility-weighted imaging in parenchymal neurosyphilis: identification of a new MRI finding. Sex Transm Infect. 2015; 91(7):489–92. [PubMed: 25834123]

37. Toh CH, et al. Differentiation of pyogenic brain abscesses from necrotic glioblastomas with use of susceptibility-weighted imaging. AJNR Am J Neuroradiol. 2012; 33(8):1534–8. [PubMed: 22422181]

38. Antulov R, et al. Differentiation of pyogenic and fungal brain abscesses with susceptibility-weighted MR sequences. Neuroradiology. 2014; 56(11):937–45. [PubMed: 25085012]

39. Bijlsma MW, et al. Community-acquired bacterial meningitis in adults in the Netherlands, 2006–14: a prospective cohort study. The Lancet Infectious Diseases. 2016; 16(3):339–347. [PubMed: 26652862]

40. Bosemani T, Poretti A, Huisman TA. Susceptibility-weighted imaging in pediatric neuroimaging. J Magn Reson Imaging. 2014; 40(3):530–44. [PubMed: 24925729]

41. Santhosh K, et al. Susceptibility weighted imaging: a new tool in magnetic resonance imaging of stroke. Clin Radiol. 2009; 64(1):74–83. [PubMed: 19070701]

42. Polan RM, et al. Susceptibility-weighted imaging in pediatric arterial ischemic stroke: a valuable alternative for the noninvasive evaluation of altered cerebral hemodynamics. AJNR Am J Neuroradiol. 2015; 36(4):783–8. [PubMed: 25477354]

43. Elnekeidy AE, Yehia A, Elfatatry A. Importance of susceptibility weighted imaging (SWI) in management of cerebro-vascular strokes (CVS). Alexandria Journal of Medicine. 2014; 50(1):83–91.

44. Moulin T, et al. Hemorrhagic infarcts. Eur Neurol. 1994; 34(2):64–77. [PubMed: 8174597]

45. Copen WA, Schaefer PW, Wu O. MR perfusion imaging in acute ischemic stroke. Neuroimaging Clin N Am. 2011; 21(2):259–83. x. [PubMed: 21640299]

46. Kao HW, Tsai FY, Hasso AN. Predicting stroke evolution: comparison of susceptibility-weighted MR imaging with MR perfusion. Eur Radiol. 2012; 22(7):1397–403. [PubMed: 22322311]

47. Miyasaka T, et al. Application of susceptibility weighted imaging (SWI) for evaluation of draining veins of arteriovenous malformation: utility of magnitude images. Neuroradiology. 2012; 54(11): 1221–7. [PubMed: 22592320]

48. Tsui YK, et al. Susceptibility-weighted imaging for differential diagnosis of cerebral vascular pathology: a pictorial review. J Neurol Sci. 2009; 287(1–2):7–16. [PubMed: 19772973]

49. George U, et al. Susceptibility-weighted imaging in the evaluation of brain arteriovenous malformations. Neurol India. 2010; 58(4):608–14. [PubMed: 20739804]

50. Lee BC, et al. MR high-resolution blood oxygenation level-dependent venography of occult (low-flow) vascular lesions. AJNR Am J Neuroradiol. 1999; 20(7):1239–42. [PubMed: 10472978]

51. Bulut HT, Sarica MA, Baykan AH. The value of susceptibility weighted magnetic resonance imaging in evaluation of patients with familial cerebral cavernous angioma. Int J Clin Exp Med. 2014; 7(12):5296–302. [PubMed: 25664034]

52. Chaudhry US, De Bruin DE, Policeni BA. Susceptibility-weighted MR imaging: a better technique in the detection of capillary telangiectasia compared with T2* gradient-echo. AJNR Am J Neuroradiol. 2014; 35(12):2302–5. [PubMed: 25147196]

53. Tamer H, et al. Hemodynamic analysis of an adult vein of Galen aneurysm malformation by use of 3D image-based computational fluid dynamics. AJNR Am J Neuroradiol. 2003; 24(6):1075–1082. [PubMed: 12812929]

54. Tong KA, et al. Susceptibility-weighted MR imaging: a review of clinical applications in children. AJNR Am J Neuroradiol. 2008; 29(1):9–17. [PubMed: 17925363]

55. Verschuuren S, et al. Susceptibility-weighted imaging of the pediatric brain. AJR Am J Roentgenol. 2012; 198(5):W440–9. [PubMed: 22528925]

56. Dai Y, et al. Visualizing cerebral veins in fetal brain using susceptibility-weighted MRI. Clin Radiol. 2014; 69(10):e392–7. [PubMed: 25060932]

57. Kelly JE, et al. Susceptibility-weighted imaging helps to discriminate pediatric multiple sclerosis from acute disseminated encephalomyelitis. Pediatr Neurol. 2015; 52(1):36–41. [PubMed: 25532777]

58. Hu J, et al. MR susceptibility weighted imaging (SWI) complements conventional contrast enhanced T1 weighted MRI in characterizing brain abnormalities of Sturge-Weber Syndrome. J Magn Reson Imaging. 2008; 28(2):300–7. [PubMed: 18666142]

59. Hingwala D, et al. Clinical utility of susceptibility-weighted imaging in vascular diseases of the brain. Neurol India. 2010; 58(4):602–7. [PubMed: 20739803]

60. Franceschi AM, et al. Use of Susceptibility-Weighted Imaging (SWI) in the Detection of Brain Hemorrhagic Metastases from Breast Cancer and Melanoma. J Comput Assist Tomogr. 2016; 40(5):803–5. [PubMed: 27636126]

61. Hsu CC, et al. Susceptibility-Weighted Imaging of Glioma: Update on Current Imaging Status and Future Directions. J Neuroimaging. 2016; 26(4):383–90. [PubMed: 27227542]

62. Daldrup-Link HE, et al. MRI of tumor-associated macrophages with clinically applicable iron oxide nanoparticles. Clin Cancer Res. 2011; 17(17):5695–704. [PubMed: 21791632]

63. Mohammed W, et al. Clinical applications of susceptibility-weighted imaging in detecting and grading intracranial gliomas: a review. Cancer Imaging. 2013; 13:186–95. [PubMed: 23618919]

64. Cha S, et al. Intracranial mass lesions: dynamic contrast-enhanced susceptibility-weighted echo-planar perfusion MR imaging. Radiology. 2002; 223(1):11–29. [PubMed: 11930044]

65. Wang X, et al. Neuronavigation-assisted trajectory planning for deep brain biopsy with susceptibility-weighted imaging. Acta Neurochir (Wien). 2016; 158(7):1355–62. [PubMed: 27165299]

66. Hertel F, et al. Susceptibility-Weighted MRI for Deep Brain Stimulation: Potentials in Trajectory Planning. Stereotact Funct Neurosurg. 2015; 93(5):303–8. [PubMed: 26202899]

67. Liu T, et al. Improved subthalamic nucleus depiction with quantitative susceptibility mapping. Radiology. 2013; 269(1):216–23. [PubMed: 23674786]

68. Wang M, et al. Susceptibility weighted imaging in detecting hemorrhage in acute cervical spinal cord injury. Magn Reson Imaging. 2011; 29(3):365–73. [PubMed: 21232894]

69. Martin N, et al. Comparison of MERGE and axial T2-weighted fast spin-echo sequences for detection of multiple sclerosis lesions in the cervical spinal cord. AJR Am J Roentgenol. 2012; 199(1):157–62. [PubMed: 22733907]

70. Ishizaka K, et al. Detection of normal spinal veins by using susceptibility-weighted imaging. J Magn Reson Imaging. 2010; 31(1):32–8. [PubMed: 20027570]

71. Katayama Y, et al. Continuous monitoring of jugular bulb oxygen saturation as a measure of the shunt flow of cerebral arteriovenous malformations. J Neurosurg. 1994; 80(5):826–33. [PubMed: 8169621]

72. Cai M, et al. Susceptibility-weighted imaging of the venous networks around the brain stem. Neuroradiology. 2015; 57(2):163–9. [PubMed: 25326168]

73. Liu T, et al. Morphology enabled dipole inversion (MEDI) from a single-angle acquisition: comparison with COSMOS in human brain imaging. Magn Reson Med. 2011; 66(3):777–83. [PubMed: 21465541]

74. Liu J, et al. Morphology enabled dipole inversion for quantitative susceptibility mapping using structural consistency between the magnitude image and the susceptibility map. Neuroimage. 2012; 59(3):2560–8. [PubMed: 21925276]

75. Schweser F, et al. Quantitative susceptibility mapping for investigating subtle susceptibility variations in the human brain. Neuroimage. 2012; 62(3):2083–100. [PubMed: 22659482]

76. Wu B, et al. Whole brain susceptibility mapping using compressed sensing. Magn Reson Med. 2012; 67(1):137–47. (1). [PubMed: 21671269]

77. Liu T, et al. Calculation of susceptibility through multiple orientation sampling (COSMOS): a method for conditioning the inverse problem from measured magnetic field map to susceptibility source image in MRI. Magn Reson Med. 2009; 61(1):196–204. [PubMed: 19097205]

78. Wharton S, Bowtell R. Whole-brain susceptibility mapping at high field: a comparison of multiple- and single-orientation methods. Neuroimage. 2010; 53(2):515–25. [PubMed: 20615474]

79. Deistung A, et al. Toward in vivo histology: a comparison of quantitative susceptibility mapping (QSM) with magnitude-, phase-, and R2*-imaging at ultra-high magnetic field strength. Neuroimage. 2013; 65:299–314. [PubMed: 23036448]

80. Khabipova D, et al. A modulated closed form solution for quantitative susceptibility mapping–a thorough evaluation and comparison to iterative methods based on edge prior knowledge. Neuroimage. 2015; 107:163–74. [PubMed: 25463463]

81. Sodickson DK, Manning WJ. Simultaneous acquisition of spatial harmonics (SMASH): fast imaging with radiofrequency coil arrays. Magn Reson Med. 1997; 38(4):591–603. [PubMed: 9324327]

82. Pruessmann KP, et al. SENSE: sensitivity encoding for fast MRI. Magn Reson Med. 1999; 42(5): 952–62. [PubMed: 10542355]

83. Griswold MA, et al. Generalized autocalibrating partially parallel acquisitions (GRAPPA). Magn Reson Med. 2002; 47(6):1202–10. [PubMed: 12111967]

84. Breuer FA, et al. Controlled aliasing in volumetric parallel imaging (2D CAIPIRINHA). Magn Reson Med. 2006; 55(3):549–56. [PubMed: 16408271]

85. Bilgic B, et al. Wave-CAIPI for highly accelerated 3D imaging. Magn Reson Med. 2015; 73(6): 2152–62. [PubMed: 24986223]

86. Moriguchi H, Duerk JL. Bunched phase encoding (BPE): a new fast data acquisition method in MRI. Magn Reson Med. 2006; 55(3):633–48. [PubMed: 16470597]

87. Zahneisen B, et al. Three-dimensional Fourier encoding of simultaneously excited slices: generalized acquisition and reconstruction framework. Magn Reson Med. 2014; 71(6):2071–81. [PubMed: 23878075]

88. Langkammer C, et al. Fast quantitative susceptibility mapping using 3D EPI and total generalized variation. Neuroimage. 2015; 111:622–30. [PubMed: 25731991]

89. Wu B, et al. Fast and tissue-optimized mapping of magnetic susceptibility and T2* with multi-echo and multi-shot spirals. Neuroimage. 2012; 59(1):297–305. [PubMed: 21784162]

90. Bilgic B, et al. Rapid multi-orientation quantitative susceptibility mapping. Neuroimage. 2016; 125:1131–41. [PubMed: 26277773]

91. de Rochefort L, et al. In vivo quantification of contrast agent concentration using the induced magnetic field for time-resolved arterial input function measurement with MRI. Med Phys. 2008; 35(12):5328–39. [PubMed: 19175092]

92. Liu Z, et al. Preconditioned total field inversion (TFI) method for quantitative susceptibility mapping. Magn Reson Med. 2016

93. Kudo K, et al. Oxygen extraction fraction measurement using quantitative susceptibility mapping: Comparison with positron emission tomography. J Cereb Blood Flow Metab. 2016; 36(8):1424–33. [PubMed: 26661168]

94. Fan AP, et al. Quantitative oxygenation venography from MRI phase. Magn Reson Med. 2014; 72(1):149–59. [PubMed: 24006229]

95. Jain V, Langham MC, Wehrli FW. MRI estimation of global brain oxygen consumption rate. J Cereb Blood Flow Metab. 2010; 30(9):1598–607. [PubMed: 20407465]

96. Haacke EM, et al. In vivo measurement of blood oxygen saturation using magnetic resonance imaging: a direct validation of the blood oxygen level-dependent concept in functional brain imaging. Hum Brain Mapp. 1997; 5(5):341–6. [PubMed: 20408238]

97. Fan AP, et al. Baseline oxygenation in the brain: Correlation between respiratory-calibration and susceptibility methods. Neuroimage. 2016; 125:920–31. [PubMed: 26549301]

98. Xu B, et al. Quantification of cerebral perfusion using dynamic quantitative susceptibility mapping. Magn Reson Med. 2015; 73(4):1540–8. [PubMed: 24733457]

99. Cetin, S., et al. Vessel Orientation Constrained Quantitative Susceptibility Mapping (QSM) Reconstruction. In: Ourselin, S., et al., editors. Medical Image Computing and Computer-Assisted Intervention – MICCAI 2016: 19th International Conference, Athens, Greece, October 17–21, 2016, Proceedings, Part III. Springer International Publishing; Cham: 2016. p. 467-474.

100. Bazin, PL., et al. Vessel segmentation from quantitative susceptibility maps for local oxygenation venography. 2016 IEEE 13th International Symposium on Biomedical Imaging (ISBI); 2016.

101. Dula AN, et al. Magnetic resonance imaging of the cervical spinal cord in multiple sclerosis at 7T. Mult Scler. 2016; 22(3):320–8. [PubMed: 26209591]

102. Barry RL, et al. Resting state functional connectivity in the human spinal cord. Elife. 2014; 3:e02812. [PubMed: 25097248]

103. Delso G, et al. Anatomic evaluation of 3-dimensional ultrashort-echo-time bone maps for PET/MR attenuation correction. J Nucl Med. 2014; 55(5):780–5. [PubMed: 24639457]

104. Sheth V, et al. Magnetic resonance imaging of myelin using ultrashort Echo time (UTE) pulse sequences: Phantom, specimen, volunteer and multiple sclerosis patient studies. Neuroimage. 2016; 136:37–44. [PubMed: 27155128]

105. Du J, et al. Ultrashort echo time (UTE) magnetic resonance imaging of the short T2 components in white matter of the brain using a clinical 3T scanner. Neuroimage. 2014; 87:32–41. [PubMed: 24188809]

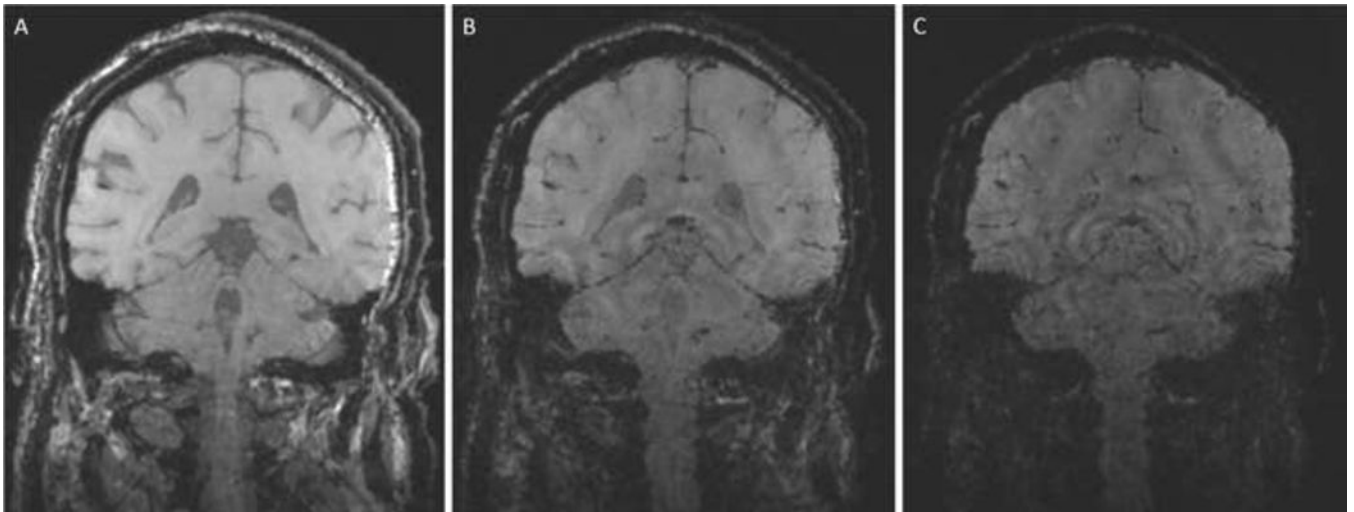106. Li W, et al. Susceptibility tensor imaging (STI) of the brain. NMR Biomed. 2016

Figure 1.
3D T2* weighted multi echo GRE images obtained at 3T. (A) TE=14, (B)TE=33, (C)
TE=52. Note that with increasing TE, the T2* contrast increases, but artifacts due to field
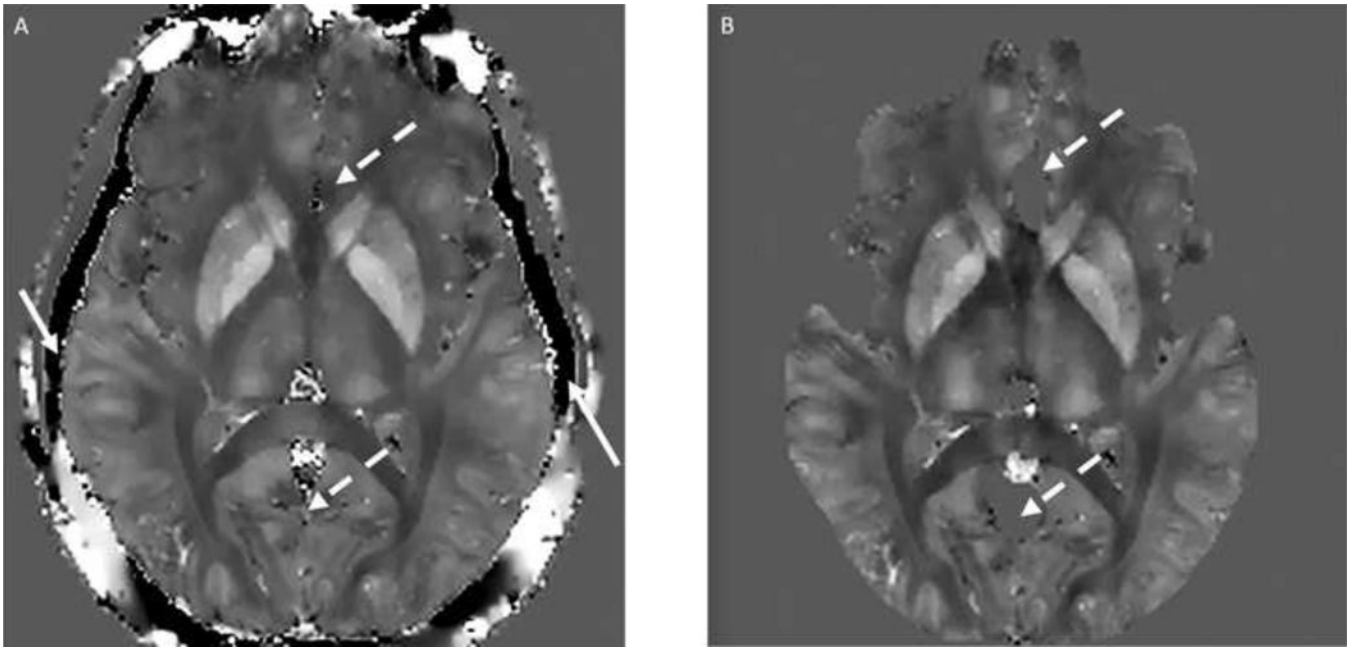inhomogeneity also increase.

Figure 2.
QSM MEDI and QSM TFI images on same subject, acquired at 3T. (A) QSM TFI (B)QSM MEDI. Note that skull anatomic landmarks (solid arrows) and brain tissue (dashed arrows) are preserved in the mask free TFI method, compared to MEDI on these images.
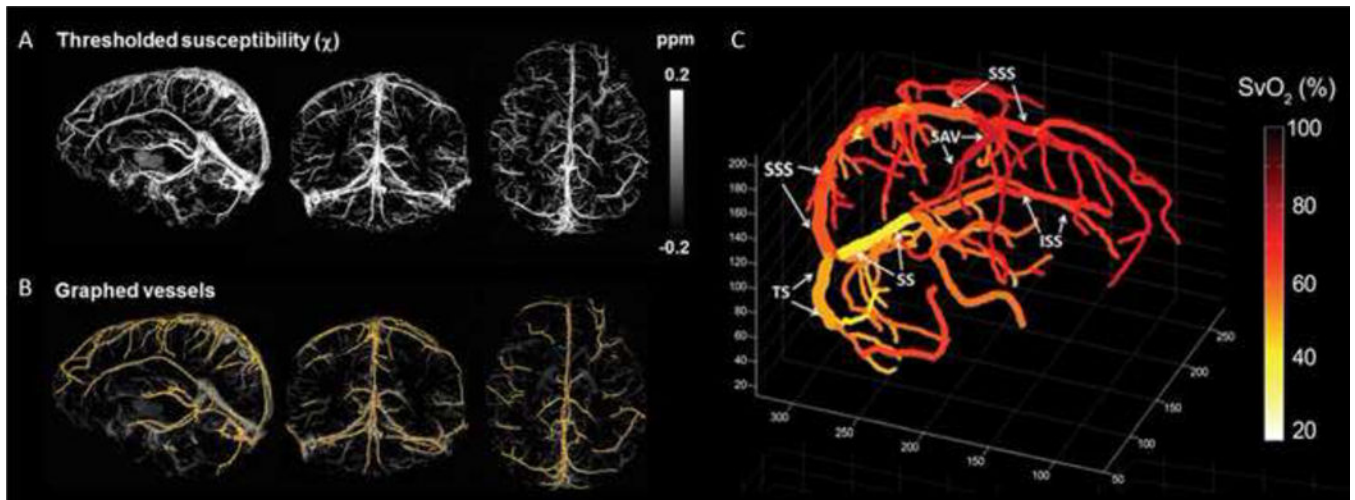
Figure 3.
QSM Venous Oxygenation Mapping. (A) Original QSM map in healthy volunteer with $\chi >$ 0.15 threshold, (B) Surface renderings of vessel and (C) Calculated Mixed Venous Oxygen Saturation measurements (SvO2). SSS=superior sagittal sinus, SS=straight sinus, TS=transverse sinus, ISS=inferior sagittal sinus, SAV=superficial anastomic vein.
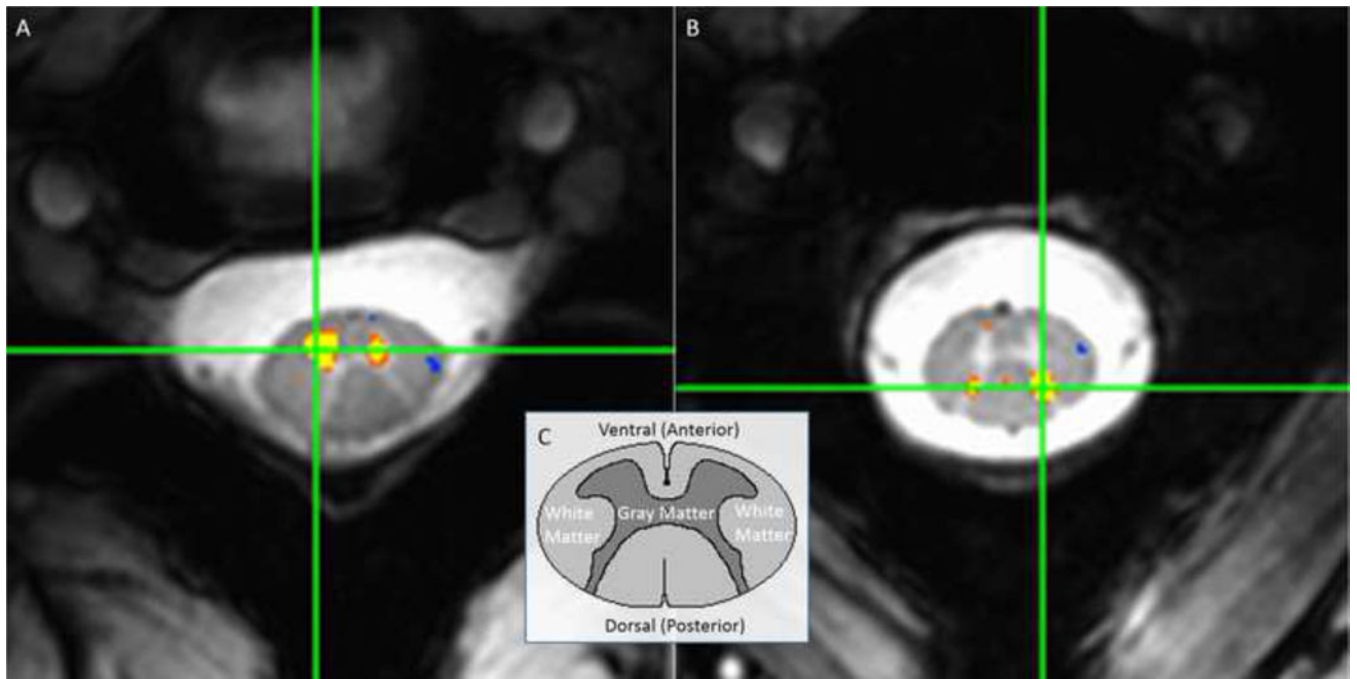
Figure 4.
7T resting state functional connectivity maps of cervical spinal cord. Functional connectivity demonstration between (A) left and right ventral (motor) horns and (B) left and right dorsal (sensory) horns of spinal cord gray matter. (C) Spinal cord gross anatomical arrangement.
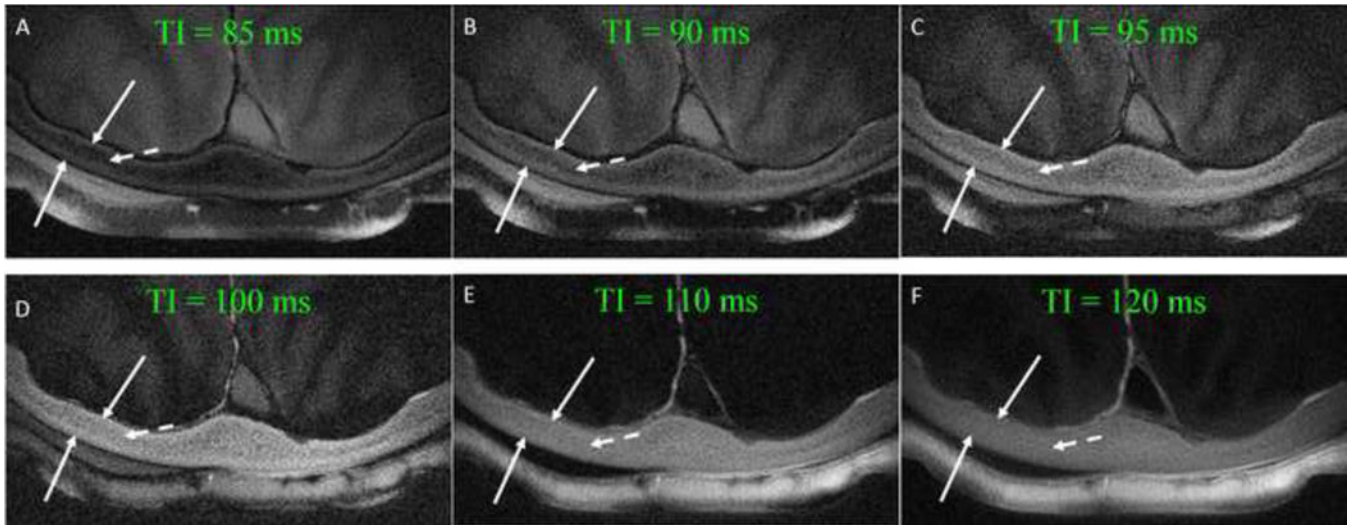
Figure 5.
Brain IR UTE MRI at varying inversion times (TI) (TR = 300, TI = 85/90/95/100/110/120 ms). Contrast between cortical bone (solid arrows) and marrow (dashed arrows) is greatest at (A) TI-85ms and least at (B) TI-120ms.

Table 1

Paramagnetic and Diamagnetic Tissue Components(Haacke and Reichenbach 2011).

Paramagnetic	Relevance	Diamagnetic	Relevance
Storage forms of iron: Fe^{+2} and Fe^{+3}: Hemosiderin; Fe^{+3}: Ferritin	Hemorrhage, Hemochromatosis	Water	
Deoxyhemoglobin	Vascular diseases	Phospholipids, myelin	Demyelinating diseases
Methemoglobin (extracellular)	Hemorrhage, Methemoglobinemia, Sickle Cell Anemia	Oxyhemoglobin	Vascular diseases
Hemosiderin (intracellular after macrophage phagocytosis)	Hemorrhage, hemochromatosis	Calcium phosphate	Vascular calcification, tumor
Ceruloplasmin (Cu^{2+} carrying enzyme)	Wilson's disease	Most organic molecules	
Gd^{3+}	Gadolinium enhancement	NaCl	
$Mn^{2+}, Co^{2+}, Cr^{2+}$			

Haacke, E. M. and J. r. R. Reichenbach (2011). Susceptibility weighted imaging in MRI : basic concepts and clinical applications. Hoboken, N.J., Wiley-Blackwell.